This article is an accepted version. Please cite the published version:

https://doi.org/10.1021/acs.nanolett.5c01332

NANO LETTERS

pubs.acs.org/NanoLett Letter

Stochastic Nature of Voltage-Controlled Charge Dynamics in AlO_x Magnetic Tunnel Junctions

Chun-Yen Chen, Bao-Huei Huang, Yu-Hui Tang,* César Gonzalez-Ruano, Farkhad G. Aliev, Dah-Chin Ling, and Jhen-Yong Hong*

Cite This: *Nano Lett.* 2025, 25, 11776−11781

Read Online

ACCESS | Metrics & More | Article Recommendations | Supporting Information

ABSTRACT: Spintronic memristors based on ferromagnetic metal/oxide heterostructures have recently enabled reversible manipulation of both magnetic properties and resistive switching (RS), offering promising prospects for multibit memory and neuromorphic computing. In this study, we investigate the stochastic nature and relaxation processes of charge dynamics induced by localized oxygen vacancy (V_O) in AlO_x-based magnetic tunnel junctions (MTJs). We observe that random telegraph noise (RTN) exhibits charge stochasticity at specific bias voltages in the low resistance state (LRS), reflecting the competition and transition between charge capture and emission states against the thermal energy. This behavior reveals that the thermally unstable charge stochasticity originates from localized traps in the AlO_x barrier. In contrast, the high resistance state (HRS) favors the RTN emission states, indicating the dominance of direct tunneling effects. Through numerical calculations based on the tight-binding (TB) model and experimental results, we demonstrate that voltage-driven shifts in the V_O position within the AlO_x barrier, associated with RS, govern the charge dynamics of the MTJs investigated. These findings provide valuable insights and practical implications for the development of next-generation devices leveraging charge stochasticity in AlO_x-based MTJs.

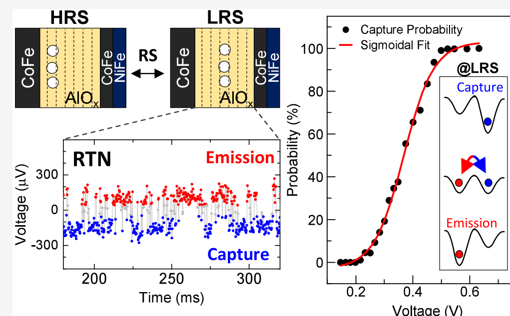

KEYWORDS: *magnetic tunnel junction, memristor, resistive switching, random telegraph noise, oxygen vacancy*

Downloaded via UNIV AUTONOMA DE MADRID on December 16, 2025 at 11:25:23 (UTC).
See https://pubs.acs.org/sharingguidelines for options on how to legitimately share published articles.

Magnetic tunnel junctions (MTJs), which serve as memory cells of magnetoresistive Random Access Memory (MRAM), are widely used due to their fast, energy-efficient, and nonvolatile data storage capabilities in information technology, as well as their sensitivity in magnetic field detection.[1,2] Compared to MRAM, which operates based on the manipulation of magnetic configurations, the memristor for resistive random-access memory (RRAM or ReRAM) is another class of nonvolatile memory that relies on resistive switching (RS). This mechanism uses electrical control to alter the oxide state and create the switchable conductive path in the oxide barrier.[3−5] Spintronic memristors, which integrate MTJ structures with memristive functionalities, offer comprehensive control through memristor properties, magnetoresistance, and spin torque configurations. These devices support multiple resistance states and hold great promise for revolutionizing nonvolatile data storage and neuromorphic computing with vast potential for groundbreaking advancements.[6−10] However, the challenge of downscaling devices remains to be addressed to enable the stable operation of subnanometer scale memristors[11,12] and interfacial magneto-ionic materials,[13−15] unless an energy barrier is sufficiently high to thermally isolate the multiresistance states.

Thermally unstable MTJs with stochastic magnetic configuration have recently been successfully proposed for an unconventional neuromorphic computing in the probabilistic-bit (p-bit).[16−19] The similar probabilistic phenomenon has also been observed in tunnel diodes[19] and RS-based memristor devices.[20,21] In principle, the central insulating oxide provides various possible electron transport paths,[5] including Schottky emission, Fowler−Nordheim tunneling, and toggling the charge trapping and detrapping. While RS is widely believed to originate from the formation and annihilation of conduction channels through the distribution of oxygen ions (O^{2-}) or oxygen vacancies (V_O), directly measuring this process remains experimentally challenging.

Recent advances in processing technology have led to significant work on nanoscale devices that have a very small active volume and contain only a limited number of charge carriers. This makes it possible to detect the alternating capture and emission of these carriers at individual trap sites by measuring the associated random telegraph noise (RTN).[22−27] In our previous studies, RS was observed in ultrathin (1.5 nm)

Received: February 27, 2025
Revised: June 13, 2025
Accepted: June 17, 2025
Published: July 1, 2025

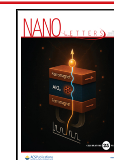

© 2025 American Chemical Society

AlO_x-based MTJs, where four resistance states can be achieved by electrical and magnetic field control.[28,29] We also found that RTN is sensitive to the spatial distribution and migration of inherent V_O, which significantly impacts spin-dependent tunneling due to different tunneling lengths.[30] However, at the subnanometer scale, a detailed understanding of V_O dynamics and its influence on transport properties remains elusive unless the exact relaxation process responsible for RTN states can be identified. To address this, precise control of the bias voltage in the RS is required to tune the energy competition between the V_O trap levels and the Fermi level against thermal energy, thereby enhancing RTN. This approach could further facilitate the investigation of charge transport characteristics and determine whether the system exhibits thermally unstable states, offering considerable potential for neuromorphic applications.

In this study, we demonstrate thermally unstable charge stochasticity and voltage-controlled charge dynamics in the AlO_x MTJs. We have extensively investigated how the stochastic nature of RTN depends on the bias voltage across different resistance states. Our results indicate that, in the low resistance state (LRS), charge capture and emission occur with stochastic features, while in the high resistance state (HRS), only charge emission is observed. Additionally, we combined the localized-trap-induced RTN with the single-band tight-binding (TB) model to qualitatively explore the voltage-driven RS as the AlO_x layer scales down to subnanometer dimensions. These findings could pave the way for the design of spintronics memristors with a stochastic neural functionality.

The $I-V$ characteristics are illustrated in Figure 1a for the initial resistance state (IRS), HRS, and LRS. Initially, an

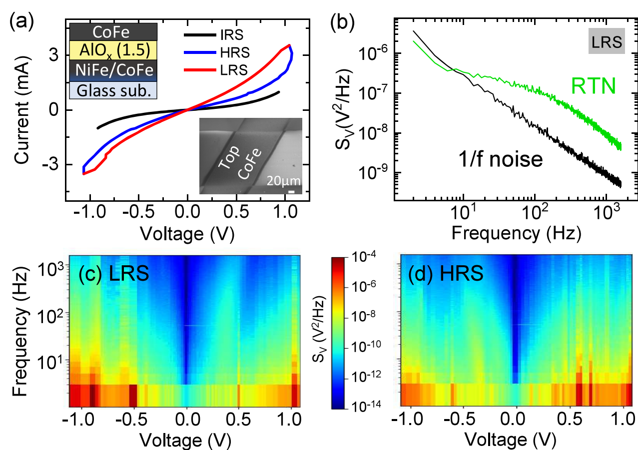

Figure 1. (a) Bipolar $I-V$ characteristics for three RS states of IRS (black), HRS (blue), and LRS (red). The upper left and lower right insets are the schematic and top-view SEM image of the MTJ, respectively. (b) Power spectral density of the voltage fluctuations (S_V) for the $1/f$ noise at +0.672 V and the RTN at +0.375 V in LRS. (c, d) Bias voltage dependence of the noise spectra for the LRS and HRS, respectively.

electroforming process must be performed on the IRS to create new conducting paths for bipolar RS, which requires opposite voltage polarities for the ON (SET) and OFF (RESET) processes.[28] The resistance is switched from HRS to LRS with a SET voltage of +1.1 V and can be returned to the HRS with a RESET voltage of −1.1 V. Since the nonlinear behavior of the $I-V$ curve indicates that the charge transport is primarily governed by the tunneling process, the low frequency noise measurement was further conducted to identify the microscopic origin of the RS between LRS and HRS. The power spectral density (S_V) of the voltage fluctuations is shown in Figure 1b for the $1/f$ noise at +0.672 V and the RTN at +0.375 V at LRS. The noise spectra of the whole bias voltage for LRS and HRS are depicted in Figure 1c,d, respectively. A local-bump in the LRS noise spectrum indicates the presence of RTN in the positive bias region (+0.5 V to +0.25 V), while for HRS, the bump occurs in the negative bias region (−0.5 V to −0.3 V). Note that all noise signals were collected simultaneously at each bias voltage.

For the LRS, we clearly observe a two-level RTN at 450, 375, and 316 mV as displayed in Figure 2a−c, respectively. To investigate the underlying mechanism, we consider a two-level system with $n + 1$ and n electrons, where E_T represents the trap energy and E_F denotes the Fermi level of the electrode in metal/oxide/metal sandwich structures. In this model, a donor trap becomes neutral upon capturing an electron (trapping) and positively charged when it emits an electron (detrapping).[31] Figure 2d shows that, experimentally, the probability of capture events decreases from 100% to 0% when the bias voltage drops from 0.6 to 0.2 V, which can be well fitted by a sigmoidal model. The relaxation time for capture ($\overline{\tau}_c$) and emission ($\overline{\tau}_e$) events in RTN can be determined by the Poisson process,[32] i.e., $P(t) = \overline{\tau}_{c,e}^{-1}\exp(-t/\overline{\tau}_{c,e})$. Figure 2e shows the characteristic time $\overline{\tau}_c$ and $\overline{\tau}_e$ as a function of bias voltage. A clear transition between $\overline{\tau}_c$ and $\overline{\tau}_e$ can be observed in the LRS as the bias voltage is gradually decreased. Such a stochastic nature in localized-trap-induced RTN in the LRS may provide new insights and implications for developing alternative electric-field-based stochastic MTJs for high-performance p-bit.[33] Notably, in the HRS, RTN is dominated by a $\overline{\tau}_e$ between −0.5 V and −0.3 V, as shown in the left side of Figure 2e, without the transition between capture and emission. This behavior is markedly different from that observed in conventional insulating-oxide-based RRAM devices, where RTN is predominantly found in the HRS and rarely in the LRS.[26,27,34] In our system, RTN is observed in both HRS and LRS, although they exhibit distinct behaviors. We believe that these differences in noise characteristics stem from the varying trap distributions in HRS and LRS, particularly within the ultrathin AlO_x tunneling barrier. The free electrons become highly sensitive in their transport due to the presence of distinct trap sites, and the tunneling effect is significantly influenced by the localized distribution of these traps.

The relationship between the energy level E_T and E_F can be further clarified by examining the logarithm of the ratio of $\overline{\tau}_c$ to $\overline{\tau}_e$,[34,35]

$$\ln(\overline{\tau}_c/\overline{\tau}_e) = \frac{E_T - E_F}{k_B T} \tag{1}$$

where E_F represents the Fermi energy of the electrode, k_B is the Boltzmann constant, and T denotes the temperature. To gain a deeper understanding of the underlying mechanisms, we first consider an electron that is trapped at an energy (E_T), located at a trap depth (Z_T),[34]

$$E_T - E_F = \phi_0 - \left[(E_C - E_T) + \left|q\frac{Z_T}{d}V_b\right|\right] \tag{2}$$

https://doi.org/10.1021/acs.nanolett.5c01332
Nano Lett. 2025, 25, 11776−11781

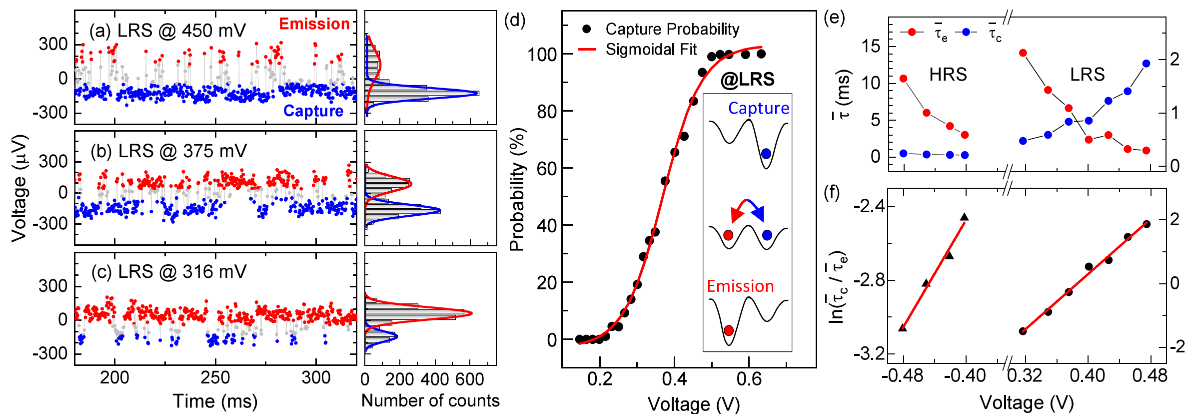

Figure 2. Time resolved RTN signals in the LRS at (a) 450 mV, (b) 375 mV, and (c) 316 mV, where blue and red dots represent capture and emission states, respectively. (d) Voltage dependence of the probability and a sigmoidal fitting of the capture event in the LRS. The inset represents the energy profile between the capture and emission events. (e) Time constant and (f) the logarithmic ratio of capture and emission time constants as a function of bias voltage. The HRS and LRS are denoted by circular and triangular symbols, respectively.

where ϕ_0 denotes the difference between the work function of the electrode and the electron affinity of the oxide, E_C is the conduction band minimum of the oxide, q is the electron charge, d is the thickness of the oxide layer, and V_b is the bias voltage. Based on the voltage dependence of $\ln(\overline{\tau}_c/\overline{\tau}_e)$, as displayed in Figure 2f for both the HRS and LRS, both Z_T and E_T can be directly extracted from eqs 2 and 1 for linear fitting, where Z_T is determined by the direction of the injected electron under the applied bias potential. For the HRS (−0.5 V to −0.3 V), we find a fitted $Z_{T(HRS)}$ = 0.279 nm relative to the top CoFe electrode and $E_{T(HRS)}$ = 0.01 eV relative to E_F = 0.0 eV. As for the LRS (+0.5 V to + 0.25 V), the fitting yields $Z_{T(LRS)}$ = 0.834 nm relative to the bottom NiFe/CoFe electrode and $E_{T(LRS)}$ = − 0.214 eV. These parameters, fitted through RTN analysis, are summarized in the schematics of the energy band diagram and bipolar resistance state switching depicted in Figure 3a,b, respectively.

Intuitively, one might think that a smaller (or larger) RTN-fitted effective E_T would assist the trap-mediated tunneling process more (or less), leading to a corresponding lower (or higher) resistance in the LRS (or HRS). However, the RTN-fitted Z_T's suggest a very different positioning of the trap states within the AlO_x barrier, which also strongly influences charge transport. To verify the competition between these two factors, we next utilize the spin-polarized single-band tight-binding (TB) model[36] to examine the voltage dependence of magnetoresistance (MR) in the IRS, HRS, and LRS and to compare these findings with experimental data, as illustrated in Figure 4.

To model the ultrathin AlO_x-based MTJs, we consider an insulating barrier (B), composed of seven atomic layers (N_{Bi} where i = 1−7) with barrier heights (Φ_{Bi} where i = 1−7), sandwiched by two semi-infinite ferromagnetic (FM) electrodes. Here i = 1 (7) refers to the insulating layer adjacent to the bottom (top) FM electrode. Based on the RTN-fitted Z_T's and E_T's, the barrier heights for all three cases are detailed in Table 1. The spin-polarized onsite energies of the FM electrodes are given as $\epsilon^{\uparrow}$ = 1.2 eV and $\epsilon^{\downarrow}$ = 2.0 eV, with the nearest-neighboring hopping energy of ξ = −0.4 eV for the whole FM/B/FM device. Our self-developed "JunPy+TB" package[37] is further employed to calculate the current density via the Landauer formula,

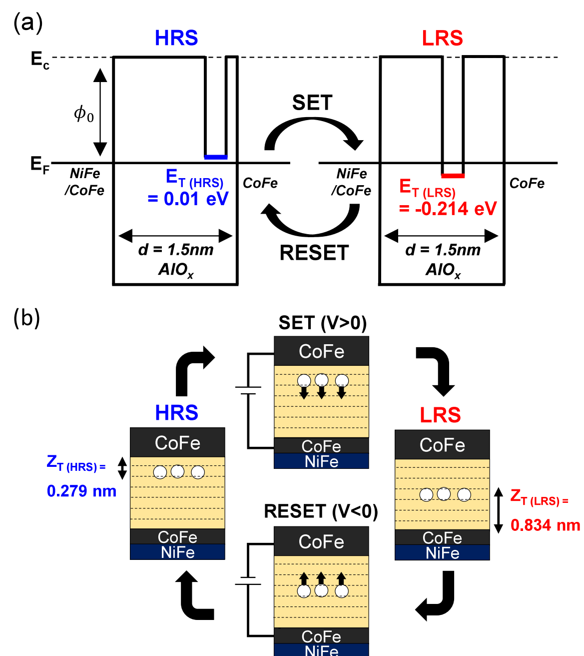

Figure 3. (a) Diagram of the energy band in the HRS and LRS, where the Fermi energy is E_F = 0.0 eV. (b) Schematics of the bipolar RS mechanism. The AlO_x barrier, consisting of seven atomic layers, as illustrated by the light yellow regions with dashed lines, is adopted for TB simulation.

$$I = \frac{e}{h}\frac{1}{\Omega_{BZ}}\int [f_t(E - eV) - f_b(E)]\mathcal{T}(E, k_{\parallel})\,dE\,dk_{\parallel} \tag{3}$$

where Ω_{BZ} represents the volume of the Brillouin zone, $f_{t(b)}$ denotes the Fermi−Dirac distribution function of the top (bottom) FM electrode, and $\mathcal{T}$ is the transmission coefficient obtained by solving the nonequilibrium Green's function (NEGF) method.[38]

The TB-calculated I−V curves for IRS, HRS, and LRS are presented in Figure 4a. We also compare the TB-calculated MR, defined as $(R_{AP} - R_P)/R_P \times 100\%$, along with the resistance ratios for the parallel (P) and antiparallel (AP) magnetic configurations, with experimental data under a bias voltage of 40 mV, as shown in Figure 4b and its inset. Here, $R_{P,AP}$ represents the resistance in the P and AP magnetic states

https://doi.org/10.1021/acs.nanolett.5c01332
Nano Lett. 2025, 25, 11776−11781

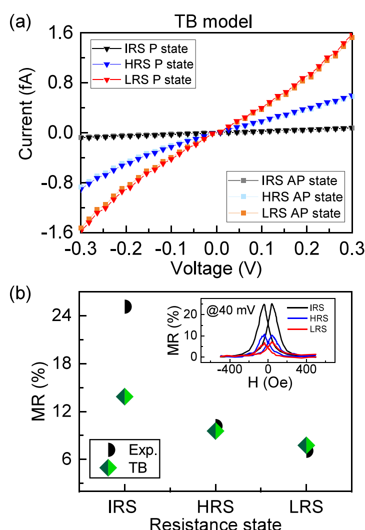

Figure 4. (a) TB-calculated $I-V$ characteristics for IRS, HRS, and LRS. (b) Comparison of magnetoresistance (MR) ratio between experimental measurement (Exp.) and TB calculation under a bias voltage at 40 mV. The inset shows the magnetic field dependence of the measured MR ratio at 40 mV.

Table 1. Barrier Heights of Insulating Barrier Used in the TB Model for IRS, HRS, and LRS Cases, where Φ_{B6} in HRS and Φ_{B4} in LRS Are Estimated by the Ratio of RTN-Fitted Z_T (HRS,LRS) to the Thickness of AlO_x (1.5 nm)[a]

	Φ_{B1}	Φ_{B2}	Φ_{B3}	Φ_{B4}	Φ_{B5}	Φ_{B6}	Φ_{B7}
IRS	1.5	1.5	1.5	1.5	1.5	1.5	1.5
HRS	1.5	1.5	1.5	1.5	1.5	**0.01**	1.5
LRS	1.5	1.5	1.5	**-0.21**	1.5	1.5	1.5

[a]Here, the energy unit is eV.

of MTJs, respectively. Notably, the excellent agreement between the TB calculations and the experimental results confirms the presence of three resistive states and suggests that the location of the trap states plays a crucial role in controlling the RS, especially in ultrathin AlO_x-based MTJs. In contrast to other oxide barriers, such as MgO, ZnO, CoO, NiO, and HfO_2, which rely on the formation of conductive filaments for memristive behavior and typically exhibit a minimal magnetic response in the LRS,[39−44] our AlO_x MTJs show a migration of localized trap sites that significantly promote the MR in LRS. This finding indicates that the MTJ studied does not conform to the conventional conductive filament type of RS but, instead, relies on the migration of interface ions/vacancies to modulate the RS-based tunneling magnetoresistance (TMR).

So far, we have successfully employed the TB model to validate our analysis of localized-trap-induced RTN. The crucial question now is: What are the traps present in the ultrathin AlO_x? Based on Figure 3a,b, it is evident that the direction of trap movement is affected by the attraction toward the negative electrode of the MTJs in bipolar RS states. This behavior suggests that the traps are likely associated with positively charged V_O states. In the HRS, the V_O state with positive and smaller E_T values is situated close to the top electrode. Conversely, in the LRS, the V_O states with negative and larger E_T are found at the center of the AlO_x layer. Notably, the information about the traps obtained through RTN analysis is consistent with the results from spin-dependent magneto-transport, as depicted in Figure 2e and Figure 4b. In the HRS, free electrons can often disregard the V_O state located at the top interface as emission events tend to dominate. This gives rise to a greater number of emission events and favors direct tunneling, thereby leading to a higher MR. In contrast, the LRS, which is characterized by transition between capture and emission processes, results in a lower MR. We propose that the V_O can be regarded as the trap medium during the tunneling process, which also explains the RTN observed in the ultrathin AlO_x barrier. From an energy perspective, E_T in the HRS lies near E_F at zero bias voltage, offering less tunability to control the transition between capture and emission states via bias voltage. However, when the localized V_O state migrates to the central region of AlO_x in the LRS, the negative $E_{T(LRS)}$ at −0.214 eV can be considered as a quantum-well state below E_F. When a bias voltage is applied between +0.2 V and +0.6 V, the difference between E_T and E_F, $E_T - E_F$, can be adjusted to near or below the thermal energy (k_BT of ∼25 meV), according to eq 2. This condition allows thermal energy to disrupt the stability of capture and emission states, leading to stochastic behavior that can be effectively modeled by a sigmoidal function. As a result, RTN is crucial for detecting stochastic charge transport dynamics, allowing us to probe the location and relative energy alignment of V_O with respect to the electrode, since the presence of V_O states also significantly affects the spin-dependent tunneling in the ultrathin AlO_x layer.

In conclusion, our study reveals that RTN in ultrathin AlO_x-based MTJs is caused by localized traps positioned at various subnanometer locations in both HRS and LRS. In particular, we identify that the thermally unstable stochastic behavior arises from the transition between capture and emission events in the LRS. This distinct configuration is attributed to stochastic charge dynamics linked to a centrally localized V_O state in ultrathin AlO_x MTJs. The "JunPy+TB" simulation, which employs RTN-fitted parameters for trap positions, shows strong agreement between the TB results and experimental measurements in MR. We demonstrate that a voltage-driven migration of V_O within the AlO_x barrier is associated with RS, leading to spin-dependent tunneling through different trap-mediated pathways for each resistive state. Our work opens new avenues for new design of neuromorphic and in-memory computing, highlighting the significant potential for applications in spintronic memristor devices.

The MTJ structure of NiFe (15 nm)/CoFe (25 nm)/AlO_x (1.5 nm)/CoFe (30 nm) was deposited on a glass substrate using dc/ac magnetron sputtering at room temperature with a base pressure of 1×10^{-8} Torr. All metallic layers were deposited by DC sputtering at a working argon pressure of $5 \times 1 \times 10^{-3}$ Torr. The top CoFe and bottom CoFe/NiFe electrodes were patterned in a cross-bar configuration, featuring a junction area of 150×150 μm^2, as illustrated in the lower right inset of Figure 1a. The top electrode functions as the hard magnetic layer, while the bottom electrode serves as the soft magnetic layer. The preparation of the AlO_x junction layer involved a two-step oxidation process of the Al layer. The first step included natural oxidation, where O_2 gas was maintained at a pressure of 200×10^{-3} Torr in the chamber. This was followed by a plasma oxidation step, during which an AC power of 100 W was applied to the sputtering gun for Al_2O_3 deposition. During this phase, the sample shutter remained closed for 5 min and then opened for an oxidation period of 30 s. For the $I-V$ curves with different oxidation

https://doi.org/10.1021/acs.nanolett.5c01332
Nano Lett. 2025, 25, 11776−11781

times, please refer to the Supporting Information. To conduct the magneto-transport measurements, the $I-V$ characteristic curve and MR effect were measured with a four-point setup. The external magnetic field was applied along the soft FM layer, and the bottom FM electrode was grounded. The voltage was generated by a Keithley 2400 source meter, and the voltage across the MTJ was measured by a DT322 DAQ Board. A homemade preamplifier (based on INA111 instrumental amplifiers) and two Stanford Research System SR 560 low noise voltage amplifiers were used to perform the DC voltage noise measurements. The output signal was sent to a Stanford Research System SR 780 spectrum analyzer for noise analysis. More detailed information about the experimental setup can be found in our previous works.[28−30]

■ ASSOCIATED CONTENT

Data Availability Statement

The data that support the findings of this study are available from the corresponding author upon reasonable request.

Supporting Information

The Supporting Information is available free of charge at https://pubs.acs.org/doi/10.1021/acs.nanolett.5c01332.

> $I-V$ curves; noise spectrum; polarity; RTN of LRS and HRS; extraction of RTN time constant using the numerical program; Poisson distribution; occupancy levels and grand partition function for RTN; tight-binding model for $I-V$ characteristics simulation (PDF)

■ AUTHOR INFORMATION

Corresponding Authors

Yu-Hui Tang − *Department of Physics, National Central University, Taoyuan City 320317, Taiwan;* orcid.org/0000-0002-3579-6753; Email: yhtang@cc.ncu.edu.tw

Jhen-Yong Hong − *Department of Physics, Tamkang University, New Taipei City 251301, Taiwan;* orcid.org/0000-0002-3690-7240; Email: jyhong@mail.tku.edu.tw

Authors

Chun-Yen Chen − *Department of Physics, National Central University, Taoyuan City 320317, Taiwan;* orcid.org/0009-0005-3320-029X

Bao-Huei Huang − *Department of Physics, National Central University, Taoyuan City 320317, Taiwan*

César Gonzalez-Ruano − *Department of Condensed Matter Physics, INC and IFIMAC, Universidad Autónoma de Madrid, Madrid 28049, Spain; Department of Electrical Engineering and Institute for Research in Technology, ICAI School of Engineering, Comillas Pontifical University, 28015 Madrid, Spain*

Farkhad G. Aliev − *Department of Condensed Matter Physics, INC and IFIMAC, Universidad Autónoma de Madrid, Madrid 28049, Spain;* orcid.org/0000-0002-1682-3306

Dah-Chin Ling − *Department of Physics, Tamkang University, New Taipei City 251301, Taiwan*

Complete contact information is available at: https://pubs.acs.org/10.1021/acs.nanolett.5c01332

Author Contributions

J.-Y.H. developed the concepts and designed the experiment. C.-Y.C., F.G.A., and J.-Y.H. designed the experimental setup. C.G.-R. assisted in experimental setup for material analysis. C.-Y.C. analyzed the data. Y.-H.T., B.-H.H., and C.-Y.C. performed the tight-binding model calculation. Y.-H. T. and J.-Y.H. conceptualized the transport dynamics. C.-Y.C., Y.-H.T., D.-C.L., and J.-Y.H. interpreted the results and drafted the manuscript. All authors discussed the results and commented on the manuscript.

Notes

The authors declare no competing financial interest.

■ ACKNOWLEDGMENTS

This work was supported by the National Science and Technology Council, Taiwan (NSTC 108-2112-M-032-003-MY2, 111-2112-M-008-025, and 112-2112-M-008-036), and the National Center for Theoretical Sciences (NCTS). The work in Madrid was supported by the Spanish Ministry of Science and Innovation (PID2021-124585NB-C32, TED2021-130196B-C22, and PID2024-155399NB-I00). F.G.A. also acknowledges financial support from the Spanish Ministry of Science and Innovation through the María de Maeztu Programme for Units of Excellence in R&D (CEX 2023-001316-M) and Comunidad de Madrid TEC-2024/TEC-380 (Mag4TIC-CM) project.

■ REFERENCES

(1) Tsymbal, E. Y.; Mryasov, O. N.; LeClair, P. R. Spin-dependent tunnelling in magnetic tunnel junctions. *J. Phys.: Condens. Matter* **2003**, *15*, R109.

(2) Bhatti, S.; Sbiaa, R.; Hirohata, A.; Ohno, H.; Fukami, S.; Piramanayagam, S. Spintronics based random access memory: a review. *Mater. Today* **2017**, *20*, 530−548.

(3) Ielmini, D.; Wong, H.-S. P. In-memory computing with resistive switching devices. *Nature electronics* **2018**, *1*, 333−343.

(4) Wang, Z.; Wu, H.; Burr, G. W.; Hwang, C. S.; Wang, K. L.; Xia, Q.; Yang, J. J. Resistive switching materials for information processing. *Nat. Rev. Mater.* **2020**, *5*, 173−195.

(5) Yang, J. J.; Strukov, D. B.; Stewart, D. R. Memristive devices for computing. *Nature Nanotechnol.* **2013**, *8*, 13−24.

(6) Wang, L.; Yang, C.; Wen, J.; Gai, S.; Peng, Y. Overview of emerging memristor families from resistive memristor to spintronic memristor. *Journal of Materials Science: Materials in Electronics* **2015**, *26*, 4618−4628.

(7) Qin, J.; Sun, B.; Zhou, G.; Guo, T.; Chen, Y.; Ke, C.; Mao, S.; Chen, X.; Shao, J.; Zhao, Y. From spintronic memristors to quantum computing. *ACS Materials Lett.* **2023**, *5*, 2197−2215.

(8) Wang, X.; Chen, Y.; Xi, H.; Li, H.; Dimitrov, D. Spintronic Memristor Through Spin-Torque-Induced Magnetization Motion. *IEEE Electron Device Lett.* **2009**, *30*, 294−297.

(9) Wang, X.; Chen, Y. Spintronic memristor devices and application. In *2010 Design, Automation & Test in Europe Conference & Exhibition (DATE 2010)*, 2010; pp 667−672.

(10) Marrows, C. H.; Barker, J.; Moore, T. A.; Moorsom, T. Neuromorphic computing with spintronics. *npj Spintronics* **2024**, *2*, 12.

(11) Waser, R.; Aono, M. Nanoionics-based resistive switching memories. *Nature materials* **2007**, *6*, 833−840.

(12) Slesazeck, S.; Mikolajick, T. Nanoscale resistive switching memory devices: a review. *Nanotechnology* **2019**, *30*, 352003.

(13) Bauer, U.; Yao, L.; Tan, A. J.; Agrawal, P.; Emori, S.; Tuller, H. L.; Van Dijken, S.; Beach, G. S. Magneto-ionic control of interfacial magnetism. *Nature materials* **2015**, *14*, 174−181.

(14) Tan, A. J.; Huang, M.; Avci, C. O.; Büttner, F.; Mann, M.; Hu, W.; Mazzoli, C.; Wilkins, S.; Tuller, H. L.; Beach, G. S. Magneto-ionic control of magnetism using a solid-state proton pump. *Nat. Mater.* **2019**, *18*, 35−41.

(15) Nichterwitz, M.; Honnali, S.; Kutuzau, M.; Guo, S.; Zehner, J.; Nielsch, K.; Leistner, K. Advances in magneto-ionic materials and perspectives for their application. *APL Materials* **2021**, *9*, 030903.

(16) Camsari, K. Y.; Sutton, B. M.; Datta, S. p. bits for probabilistic spin logic. *Applied Physics Reviews* **2019**, *6*, 011305.

(17) Borders, W. A.; Pervaiz, A. Z.; Fukami, S.; Camsari, K. Y.; Ohno, H.; Datta, S. Integer factorization using stochastic magnetic tunnel junctions. *Nature* **2019**, *573*, 390−393.

(18) Hayakawa, K.; Kanai, S.; Funatsu, T.; Igarashi, J.; Jinnai, B.; Borders, W. A.; Ohno, H.; Fukami, S. Nanosecond Random Telegraph Noise in In-Plane Magnetic Tunnel Junctions. *Phys. Rev. Lett.* **2021**, *126*, 117202.

(19) Misra, S.; Bland, L. C.; Cardwell, S. G.; Incorvia, J. A. C.; James, C. D.; Kent, A. D.; Schuman, C. D.; Smith, J. D.; Aimone, J. B. Probabilistic Neural Computing with Stochastic Devices. *Adv. Mater.* **2023**, *35*, 2204569.

(20) Woo, K. S.; Kim, J.; Han, J.; Kim, W.; Jang, Y. H.; Hwang, C. S. Probabilistic computing using Cu0.1Te0.9/HfO2/Pt diffusive memristors. *Nat. Commun.* **2022**, *13*, 5762.

(21) Valle, J. d.; Salev, P.; Gariglio, S.; Kalcheim, Y.; Schuller, I. K.; Triscone, J.-M. Generation of Tunable Stochastic Sequences Using the Insulator−Metal Transition. *Nano Lett.* **2022**, *22*, 1251−1256.

(22) Ralls, K. S.; Skocpol, W. J.; Jackel, L. D.; Howard, R. E.; Fetter, L. A.; Epworth, R. W.; Tennant, D. M. Discrete Resistance Switching in Submicrometer Silicon Inversion Layers: Individual Interface Traps and Low-Frequency(1/*f*?) Noisey. *Phys. Rev. Lett.* **1984**, *52*, 228−231.

(23) Ielmini, D.; Nardi, F.; Cagli, C. Resistance-dependent amplitude of random telegraph-signal noise in resistive switching memories. *Appl. Phys. Lett.* **2010**, *96*, 053503.

(24) Zhang, Y.; Wu, H.; Wu, M.; Deng, N.; Yu, Z.; Zhang, J.; Qian, H. Random telegraph noise analysis in AlOx/WOy resistive switching memories. *Appl. Phys. Lett.* **2014**, *104*, 103507.

(25) Ambrogio, S.; Balatti, S.; Cubeta, A.; Calderoni, A.; Ramaswamy, N.; Ielmini, D. Statistical Fluctuations in HfOx Resistive-Switching Memory: Part II—Random Telegraph Noise. *IEEE Trans. Electron Devices* **2014**, *61*, 2920−2927.

(26) Yu, S.; Jeyasingh, R.; Wu, Y.; Wong, H.-S. P. Characterization of low-frequency noise in the resistive switching of transition metal oxide HfO_2. *Phys. Rev. B* **2012**, *85*, 045324.

(27) Choi, S.; Yang, Y.; Lu, W. Random telegraph noise and resistance switching analysis of oxide based resistive memory. *Nanoscale* **2014**, *6*, 400−404.

(28) Hong, J.-Y.; Hung, C.-F.; Yang, K.-H. O.; Chiu, K.-C.; Ling, D.-C.; Chiang, W.-C.; Lin, M.-T. Electrically programmable magnetoresistance in AlO_x-based magnetic tunnel junctions. *Sci. Rep.* **2021**, *11*, 6027.

(29) Hong, J.-Y.; Chen, C.-Y.; Ling, D.-C.; Martínez, I.; González-Ruano, C.; Aliev, F. G. Low-Frequency 1/f Noise Characteristics of Ultra-Thin AlOx-Based Resistive Switching Memory Devices with Magneto-Resistive Responses. *Electronics* **2021**, *10*, 2525.

(30) Chen, C.-Y.; Gonzalez-Ruano, C.; Martinez, I.; Aliev, F. G.; Ling, D.-C.; Tang, Y.-H.; Hong, J.-Y. Bias polarity dependent low-frequency noise in ultra-thin AlOx-based magnetic tunnel junctions. *Sci. Rep.* **2024**, *14*, 13664.

(31) Grasser, T. Stochastic charge trapping in oxides: From random telegraph noise to bias temperature instabilities. *Microelectronics Reliability* **2012**, *52*, 39−70.

(32) Soni, R.; Meuffels, P.; Petraru, A.; Weides, M.; Kügeler, C.; Waser, R.; Kohlstedt, H. Probing Cu doped Ge0.3Se0.7 based resistance switching memory devices with random telegraph noise. *J. Appl. Phys.* **2010**, *107*, 024517.

(33) Kobayashi, K.; Borders, W. A.; Kanai, S.; Hayakawa, K.; Ohno, H.; Fukami, S. Sigmoidal curves of stochastic magnetic tunnel junctions with perpendicular easy axis. *Appl. Phys. Lett.* **2021**, *119*, 132406.

(34) Lee, J.-K.; Lee, J.-W.; Park, J.; Chung, S.-W.; Roh, J. S.; Hong, S.-J.; Cho, I.-w.; Kwon, H.-I.; Lee, J.-H. Extraction of trap location and energy from random telegraph noise in amorphous TiOx resistance random access memories. *Appl. Phys. Lett.* **2011**, *98*, 143502.

(35) Kirton, M.; Uren, M. Noise in solid-state microstructures: A new perspective on individual defects, interface states and low-frequency (1/f) noise. *Adv. Phys.* **1989**, *38*, 367−468.

(36) Tang, Y.-H.; Kioussis, N.; Kalitsov, A.; Butler, W. H.; Car, R. Influence of asymmetry on bias behavior of spin torque. *Phys. Rev. B* **2010**, *81*, 054437.

(37) https://labstt.phy.ncu.edu.tw/junpy.

(38) Tang, Y.-H.; Huang, Z.-W.; Huang, B.-H. Analytic expression for the giant fieldlike spin torque in spin-filter magnetic tunnel junctions. *Phys. Rev. B* **2017**, *96*, 064429.

(39) Krzysteczko, P.; Reiss, G.; Thomas, A. Memristive switching of MgO based magnetic tunnel junctions. *Appl. Phys. Lett.* **2009**, *95*, 112508.

(40) Schulman, A.; Paz, E.; Böhnert, T.; Jenkins, A. S.; Ferreira, R. Exploring Multifunctionality in MgO-Based Magnetic Tunnel Junctions with Coexisting Magnetoresistance and Memristive Properties. *Adv. Funct. Mater.* **2023**, *33*, 2305238.

(41) Li, X.; Jia, J.; Li, Y.; Bai, Y.; Li, J.; Shi, Y.; Wang, L.; Xu, X. Realization of resistive switching and magnetoresistance in ZnO/ZnO-Co composite materials. *Sci. Rep.* **2016**, *6*, 31934.

(42) Yang, Z.; Zhan, Q.; Zhu, X.; Liu, Y.; Yang, H.; Hu, B.; Shang, J.; Pan, L.; Chen, B.; Li, R.-W. Tunneling magnetoresistance induced by controllable formation of Co filaments in resistive switching Co/ZnO/Fe structures. *Europhys. Lett.* **2014**, *108*, 58004.

(43) Zhao, D.; Qiao, S.; Luo, Y.; Chen, A.; Zhang, P.; Zheng, P.; Sun, Z.; Guo, M.; Chiang, F.-k.; Wu, J. others Magnetoresistance behavior of conducting filaments in resistive-switching NiO with different resistance states. *ACS Appl. Mater. Interfaces* **2017**, *9*, 10835−10846.

(44) Otsuka, S.; Hamada, Y.; Ito, D.; Shimizu, T.; Shingubara, S. Magnetoresistance of conductive filament in Ni/HfO2/Pt resistive switching memory. *Jpn. J. Appl. Phys.* **2015**, *54*, 05ED02.